

Defect-aware Hybrid Prompt Optimization via Progressive Tuning for Zero-Shot Multi-type Anomaly Detection and Segmentation

Nadeem Nazer Hongkuan Zhou Lavdim Halilaj Ylli Sadikaj Steffen Staab

Abstract

Recent vision language models (VLMs) like CLIP have demonstrated impressive anomaly detection performance under significant distribution shift by utilizing high-level semantic information through text prompts. However, these models often neglect fine-grained details, such as which kind of anomalies, like “hole”, “cut”, “scratch” that could provide more specific insight into the nature of anomalies. We argue that recognizing fine-grained anomaly types 1) enriches the representation of “abnormal” with structured semantics, narrowing the gap between coarse anomaly signals and fine-grained defect categories; 2) enables manufacturers to understand the root causes of the anomaly and implement more targeted and appropriate corrective measures quickly. While incorporating such detailed semantic information is crucial, designing handcrafted prompts for each defect type is both time-consuming and susceptible to human bias. For this reason, we introduce DAPO, a novel approach for **Defect-aware Prompt Optimization** based on progressive tuning for the zero-shot multi-type and binary anomaly detection and segmentation under distribution shifts. Our approach aligns anomaly-relevant image features with their corresponding text semantics by learning hybrid defect-aware prompts with both fixed textual anchors and learnable token embeddings. We conducted experiments on public benchmarks (MPDD, Visa, MVTec-AD, MAD, and Real-IAD) and an internal dataset. The results suggest that compared to the baseline models, DAPO achieves a 3.7% average improvement in AUROC and average precision metrics at the image level under distribution shift, and a 6.5% average improvement in localizing novel anomaly types under zero-shot settings.

1. Introduction

Visual inspection is a crucial task in manufacturing, ensuring that the products are free of defects before reaching customers. Manual efforts in such inspections incur high labor costs and attention. With advancements in deep learning and computer vision techniques, these complex processes are increasingly being automated, reducing manual

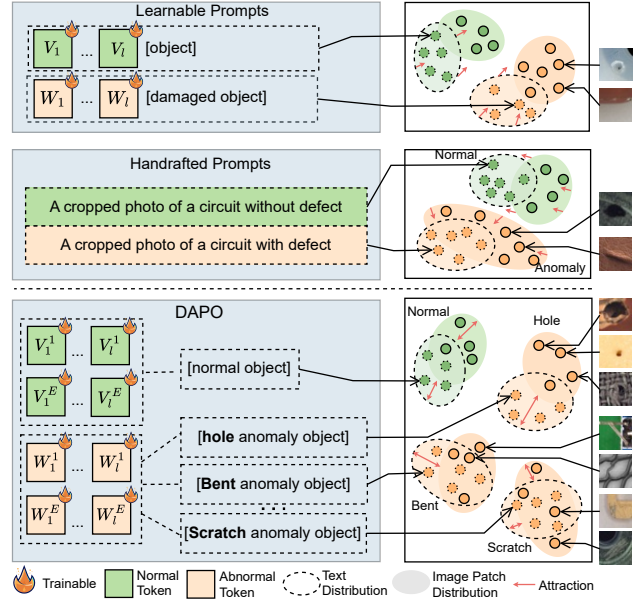


Figure 1. Existing methods (top) produce embeddings with insufficient fine-grained discriminability, suppressing cues needed to separate anomalies from normal patterns. DAPO (bottom) improves embedding representations through defect-aware progressive learning, refining them into fine-grained clusters across defect types without significant manual prompt engineering.

involvement and enabling high-precision identification of defects. Therefore, visual inspection through anomaly detection (AD) and segmentation is essential in identifying and localizing defective regions.

Most conventional approaches have adopted one-class or unsupervised anomaly detection [5, 7, 27, 33, 44], where they are trained solely on the volumes of normal (non-defective) images and classify any deviation from the learned distribution as an anomaly. Although such models perform well on their training distribution, the domain shift in industrial settings is large, so that these models often need to be trained separately on different domains or frequently retrained. Consequently, recent work increasingly leverages large-scale pre-trained VLMs (e.g., CLIP [26]), using their broad priors as an adaptable foundation that mitigates data scarcity and reduces extensive domain-specific annotation.

Despite their potential, existing approaches focus on the identification of coarse-grained anomalies, i.e., detection of an anomaly without distinguishing between fine-grained types. This limitation is critical, as 1) type-level semantics provide an inductive bias that aligns local features with defect-specific prototypes, improving robustness under distribution shift [28]; 2) focusing on the nature of anomalies such as stains, holes, or missing components is essential for industrial operators to trace root causes and implement preventive measures. MultiADS [28] attempts to address this using hand-crafted prompts and a knowledge base; but the process is time-consuming and difficult to scale for new anomalies. This highlights the need for a more flexible approach that can learn and integrate fine-grained information without relying on hand-crafted interventions.

A straightforward approach to consider is the prompt-learning technique [13, 19], which methods such as AnomalyCLIP [41] leveraged. However, directly applying such methods for fine-grained defect identification in a zero-shot scenario presents various challenges. In these tasks, a model trained on a source dataset is directly evaluated on a different target dataset, which may contain unseen defect types on various objects. Consequently, misalignment occurs with new unseen defects when learning prompt token embeddings for each prior known defect, since these embeddings for unseen defects are undefined. Additionally, CLIP suffers from an inherent modality gap rooted in an information imbalance during pre-training [29]. This causes the model to favor abstract concepts over the fine-grained visual features essential for defect-type identification. While [29] shows that enriching text descriptions during pre-training can mitigate this gap, the issue persists when applying the pre-trained model to specific downstream tasks. To overcome these challenges, we propose DAPO, **D**efect-**a**ware **P**rompt **O**ptimization, where we learn hybrid prompts for each defect type, which consists of a set of shared learnable defect token embeddings with the literal tokens of specific defect type in textual format. The objective is to have shared learnable parameters such that the same set of learnable abnormal tokens can be shared across different defect categories, so that the prompt for the new defect types can be constructed with these learnable token embeddings plus the textual description of the new defect types. The main contributions of this work are as follows:

- We propose a new method that composes prompts from fixed textual anchors plus a small set of shared, learnable defect tokens reused across defect types, removing perfect prompt engineering and enabling zero-shot construction of prompts for novel defects.
- We conduct comprehensive experiments on five publicly available industrial datasets and an internal semiconductor dataset, covering diverse object classes and significant distribution shifts. The results show that our approach

achieves superior performance in both zero-shot multi-type anomaly segmentation and binary anomaly detection under distribution shift conditions. The code base is available in the supplementary material.

2. Related Works

Unsupervised Unimodal Approaches model normal distributions from training data, treating deviations as anomalies. Reconstruction-based methods [24, 30, 33], leverage architectures of GAN [8], Variational AEs [16], and AEs [18] to find anomalies. Other approaches, such as PatchCore [27], PaDIM [5], and SPADE [4], adopt representational or memory-bank-based strategies by storing normal image features and measuring distances between test samples and those reference features using different distance measurement techniques. STPM [44] and RD4AD [7] utilize a knowledge distillation-based student-teacher framework for AD, using feature matching performed utilizing a pre-trained classification model. Anomalies are detected by measuring feature discrepancies between the student and teacher networks. However, these methods face several limitations, including dependence on training data and a one-class classification focus. These challenges motivated the development of zero-shot approaches.

Zero-Shot Anomaly Detection is gaining attention due to advancements in large-scale vision-language models (VLMs), which have wide application in robotics [34–36] and autonomous driving [37, 42]. CLIP, in particular, is serving as a widely adopted backbone for this task because of its strong zero-shot visual recognition capability. Several approaches emerged, adapting CLIP for AD, such as WinClip [11], which uses manually crafted normal and abnormal state prompts with a window-based segmentation approach. April-GAN [3] introduces additional trainable linear layers to adapt CLIP for AD. Drawing inspiration from prompt learning success in NLP, methods such as CoOp [39] and CoCoOp [38] learn task-specific prompts. AnomalyClip [41], replaces manually defined prompts with learnable object-agnostic tokens to form a general text representation for normal and abnormal classes. Similarly, SimClip [6] uses implicit prompt tuning to refine text embeddings for a better alignment between CLIP’s patch features, and AdaClip [2] combines static and dynamic prompts in a hybrid learning framework. More recently, ClipSAM [20] introduced a novel multi-modal approach by integrating CLIP with the Segment Anything Model (SAM) [17] for enhanced anomaly segmentation and detection capabilities. However, all these methods focus on learning or crafting prompts that can capture only coarse-grained features, failing to identify anomalies with different specific types. FiLo [9] introduces fine-grained anomaly descriptors generated by LLMs and adaptively

learn textual templates, replacing general “abnormal” semantics with category-specific descriptions. FAPrompt [43] learns prompts for fine-grained feature extraction but lacks alignment with different defect types. A major limitation across these approaches is their binary focus, distinguishing between only anomaly or not. MultiADS [28] represents the first attempt to address multi-defect type detection, though it relies heavily on extensive hand-crafted prompts.

Our approach overcomes these limitations by learning defect-aware prompts and effectively aligning them with local visual features, thus reducing the modality gap between these representations.

3. Preliminaries

We provide the formal definition of three anomaly detection tasks addressed in this work: (1) binary anomaly detection, (2) binary anomaly segmentation under distribution shift, and (3) zero-shot multi-type anomaly segmentation. Note that the task of binary anomaly detection/segmentation under distribution shift is commonly referred to as *zero-shot* anomaly detection/segmentation in the literature. However, we argue that this term is *misleading*, as the objective is not to locate new types of anomalies, but to distinguish between normal and anomalous samples when applied to previously unseen products (distribution shift).

Binary Anomaly Detection under Distribution Shift

Let $\mathcal{D}_{\text{train}} = \{(\mathbf{x}_i, y_i)\}_{i=1}^{N_1}$ and $\mathcal{D}_{\text{target}} = \{(\mathbf{x}_i, y_i)\}_{i=N_1+1}^{N_1+N_2}$, be two image-label datasets. They are drawn from the different input distributions $\mathcal{P}(\mathcal{X}), \mathcal{P}(\mathcal{X}')$. Specifically, $\forall i \in \{1, \dots, N_1\}, \mathbf{x}_i \sim \mathcal{P}(\mathcal{X})$ and $\forall i \in \{N_1+1, \dots, N_1+N_2\}, \mathbf{x}_i \sim \mathcal{P}(\mathcal{X}')$, where $\mathcal{P}(\mathcal{X}) \approx \mathcal{P}(\mathcal{X}')$. Each image $\mathbf{x} \in \mathbb{R}^{H \times W \times 3}$ is labeled with $y \in \{0, 1\}$, indicating anomaly presence. A binary detector $\hat{f}(\cdot)$ is trained solely on $\mathcal{D}_{\text{train}}$. At test time, the trained detector $\hat{f}(\cdot)$ is adapted to $\hat{f}'(\cdot)$ based on auxiliary target-domain-specific metadata available, such as defect information. For each $\mathbf{x} \in \mathcal{D}_{\text{target}}$, the detector $\hat{f}'(\cdot)$ classifies it as normal or anomalous.

Binary Anomaly Segmentation under Distribution Shift
 Let $\mathcal{D}_{\text{train}} = \{(\mathbf{x}_i, \mathbf{y}_i)\}_{i=1}^{N_1}$ and $\mathcal{D}_{\text{target}} = \{(\mathbf{x}_i, \mathbf{y}_i)\}_{i=N_1+1}^{N_1+N_2}$ denote the training and target datasets. The input images are drawn from different distributions $\mathcal{P}(\mathcal{X}), \mathcal{P}(\mathcal{X}')$. Specifically, $\forall i \in \{1, \dots, N_1\}, \mathbf{x}_i \sim \mathcal{P}(\mathcal{X})$ and $\forall i \in \{N_1+1, \dots, N_1+N_2\}, \mathbf{x}_i \sim \mathcal{P}(\mathcal{X}')$, where $\mathcal{P}(\mathcal{X}) \approx \mathcal{P}(\mathcal{X}')$. Each image $\mathbf{x} \in \mathbb{R}^{H \times W \times 3}$ is paired with a binary mask $\mathbf{y} \in \{0, 1\}^{H \times W}$ that indicates the presence of anomalies at each pixel. The segmentation model $\hat{f}(\cdot)$ is solely trained on $\mathcal{D}_{\text{train}}$. At test time, the trained detector $\hat{f}(\cdot)$ is adapted to $\hat{f}'(\cdot)$ based on auxiliary target-domain-specific metadata available, such as defect information. For each pixel of $\mathbf{x} \in \mathcal{D}_{\text{target}}$, the segmentation model $\hat{f}'(\cdot)$ should classify it as normal or anomalous.

Zero-shot Multi-type Anomaly Segmentation

Let $\mathcal{D}_{\text{train}} = \{(\mathbf{x}_i, \mathbf{Y}_i)\}_{i=1}^{N_1}$ and $\mathcal{D}_{\text{target}} = \{(\mathbf{x}_i, \mathbf{Y}'_i)\}_{i=N_1+1}^{N_1+N_2}$ denote two datasets with different input distributions $\mathcal{P}(\mathcal{X}), \mathcal{P}(\mathcal{X}')$. Specifically, $\forall i \in \{1, \dots, N_1\}, \mathbf{x}_i \sim \mathcal{P}(\mathcal{X})$ and $\forall i \in \{N_1+1, \dots, N_1+N_2\}, \mathbf{x}_i \sim \mathcal{P}(\mathcal{X}')$, where $\mathcal{P}(\mathcal{X}) \approx \mathcal{P}(\mathcal{X}')$. In $\mathcal{D}_{\text{train}}$, each image $\mathbf{x} \in \mathbb{R}^{H \times W \times 3}$ is paired with a mask $\mathbf{Y} \in \{0, 1\}^{H \times W \times (K_1+1)}$ encoding one normal class and K_1 defect types $\{d_1, \dots, d_{K_1}\}$, while in $\mathcal{D}_{\text{target}}$, each \mathbf{x} is labeled with $\mathbf{Y}' \in \{0, 1\}^{H \times W \times (K_2+1)}$ encoding one normal class and K_2 defect types. The segmentation model $\hat{f}(\cdot)$ is trained solely on $\mathcal{D}_{\text{train}}$. At test time $\hat{f}(\cdot)$ is adapted to $\hat{f}'(\cdot)$ based on the external knowledge of defect types in the target dataset. The model $\hat{f}'(\cdot)$ aims to predict a mask $\hat{\mathbf{Y}} \in \{0, 1\}^{H \times W \times (K_2+1)}$ that locates anomalies of different types for each $\mathbf{x} \in \mathcal{D}_{\text{target}}$.

4. Methodology

We propose Defect-Aware Prompt Optimization (DAPO), a CLIP-based approach for AD and zero-shot defect-type localization in manufacturing domains. The method leverages defect-aware learnable prompts to guide the model’s attention to visually irregular regions. As illustrated in Figure 2, a novel defect-aware prompt optimization module is used to capture fine-grained anomaly features by aligning them with multiple defect types. Given an image x , the image encoder produces a global image embedding, representing the overall semantics of the image, and patch-level embeddings, representing the local information of the given image. Instead of manually crafting prompts, we adopt a hybrid design that combines learnable tokens with human-readable tokens, capturing different defect types. During training on an auxiliary AD dataset, these prompts are optimized to maximize the similarity between the image and corresponding text embeddings. During inference, this design allows for the zero-shot localization of new anomalies by simply incorporating their textual descriptions into the prompt structure, enabling the model to generalize to defect types unseen during training.

4.1. Defect-Aware Prompt Design

Most existing AD approaches using CLIP under distribution shift relies on simple hand-crafted or learnable prompts such as “A photo of a [CLS] with anomaly”, or $P^D = [V_1][V_2] \dots [V_E][\text{damaged}][\text{CLS}]$, where [CLS] means object or class information. Although this is effective for generic AD, these prompt templates lack the expressiveness to capture fine-grained anomaly semantics and tend to focus on coarse-grained visual features, limiting their ability to distinguish between distinct defect types.

A trivial workaround to capture fine-grained semantics using CLIP is to use an ensemble of manually crafted prompts that associate different defect types with object class, as done in [28], e.g., “A photo of a [CLS] with a

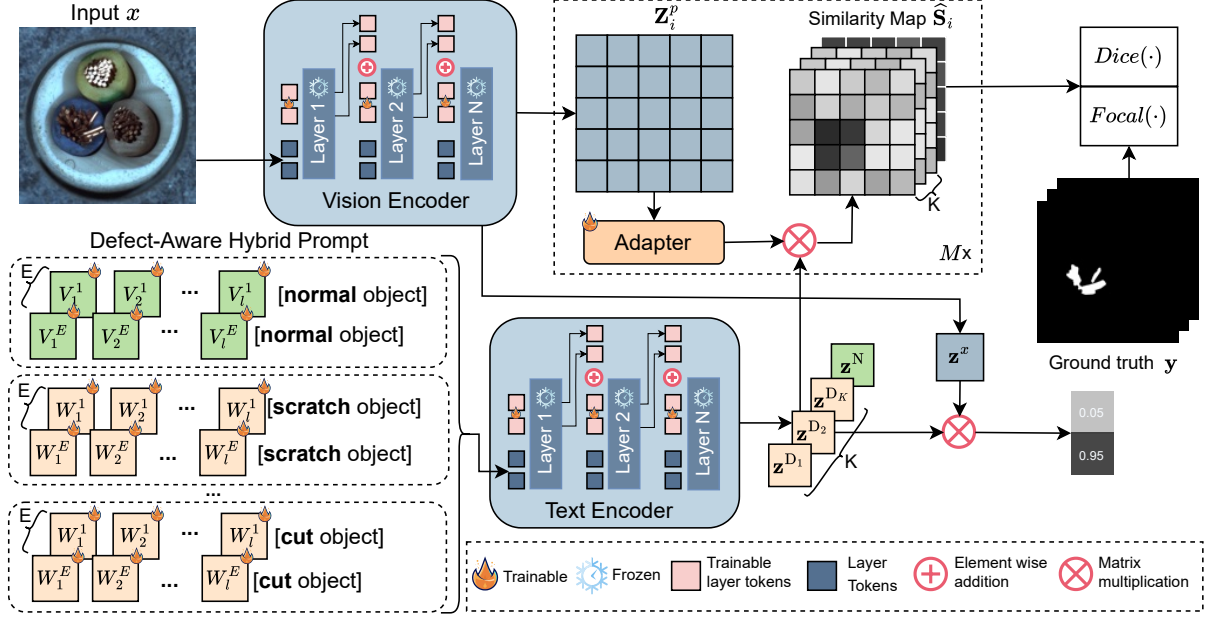


Figure 2. Overview of the proposed Defect-Aware Prompt Learning (DAPO) architecture. To enable zero-shot multi-type anomaly detection and segmentation, we progressively optimize a set of shared learnable prompts to align image features with defect-aware semantic representations. DAPO adapts pre-trained vision-language models to industrial scenarios by conditioning prompts on both global and local visual features. The shared prompt tokens are updated through a global learning strategy and reused across image patches, enabling the model to distinguish between normal and multiple defect types under distribution shifts.

cut defect”. However, creating such a comprehensive set of prompts for all possible defect-object combinations is impractical and requires significant prompt engineering effort.

To address these limitations, this paper proposes a defect-aware learnable prompts, which contain both human-readable words and learnable embeddings that can effectively capture abnormal and normal states, see Figure 2 Defect-Aware Prompt module. Specifically, the prompt for the abnormal state is composed as:

$$\mathbf{P}^D = [W_1][W_2] \dots [W_l] < \mathbf{D} > [\text{anomaly}][\text{object}], \quad (1)$$

where $[W_i], i \in \{1, 2, \dots, l\}$ are learnable context tokens. These tokens are aimed to learn a general yet effective contextual representation that represents the abnormal states. $< \mathbf{D} >$ is a placeholder for the defect-types, such as $\{\text{"bent"}, \text{"spot"}, \text{"contamination"}, \dots\}$. $[\text{anomaly}]$ and $[\text{object}]$ represent the literal tokens for the text “anomaly” and “object”, respectively. The principle is that the same learnable tokens $[W_1]$ to $[W_l]$ are shared between all types of defect. This means a single set of parameters are optimized to produce a defect-aware context that works effectively when combined with specific defect terms. The explicit $< \mathbf{D} >$ terms (“scratch”, “crack”, “bent”) provide specific defect information, while the shared learnable tokens contribute learned contextual knowledge that improves the detection across defect categories. The fixed term “anomaly” serves as a semantic anchor that leverage CLIP’s pre-trained un-

derstanding of anomalous patterns, and the “object” term maintains object-level context while allowing the learned tokens to focus on defect patterns that generalize across object categories [41]. This parameter-sharing design is computationally efficient, as it avoids learning separate contextual representations for each defect type while maintaining effectiveness across diverse anomaly categories and object classes. Similarly, the normal prompt can be represented as:

$$\mathbf{P}^N = [V_1][V_2] \dots [V_l][\text{normal}][\text{object}], \quad (2)$$

where $[V_i], i \in \{1, 2, \dots, l\}$ are learnable context tokens for normal state. Building on this foundation, to further enhance the representation capability, for one normal and K abnormal states of different defect types, we generate E prompts, each capturing different aspects of the anomaly space. For any given defect type, all E prompts are utilized, meaning that a single defect type (e.g., “scratch”) is described through E different learnable contextual embeddings. The prompt set can be written as:

$$\begin{aligned} \mathcal{B} &= \{\mathbf{P}_1^N, \mathbf{P}_2^N, \dots, \mathbf{P}_E^N\}, \\ \mathcal{A}_j &= \{\mathbf{P}_1^{D_j}, \mathbf{P}_2^{D_j}, \dots, \mathbf{P}_E^{D_j}\}, \end{aligned} \quad (3)$$

where \mathcal{B} is the prompt set for the normal state, while \mathcal{A}_j is the prompt set for the abnormal state of the j -th defect.

4.2. Prompt Optimization

Instead of finetuning the parameters of the network, we optimize the prompts set we defined in the given Equation (3). In the following section, we discuss the encoding process of images and texts and the loss function design for local and global optimization.

4.2.1. Image Encoding

Given an input image $\mathbf{x} \in \mathbb{R}^{H \times W \times 3}$, the image encoder generates intermediate image patch embeddings at M encoding stages or layers and a single global image embedding \mathbf{z}^x in the shared vision-text semantic space \mathcal{Z} . For each stage $i \in \{1, 2, \dots, M\}$, a linear adapter transforms the corresponding patch embeddings into the vision-text semantic space \mathcal{Z} . We denote these adapted embeddings as $\mathbf{Z}_i^p \in \mathbb{R}^{C \times H' \times W'}$. $H' \times W'$ are the resolution of image patch embeddings. Formally, the output of the image encoder is defined by:

$$(\mathbf{z}^x, \mathbf{Z}_1^p, \dots, \mathbf{Z}_M^p) = f_\theta(\mathbf{x}), \quad (4)$$

where $f_\theta(\cdot)$ is the parameterized image encoder function.

4.2.2. Text Encoding

For each prompt $\mathbf{P} \in \mathcal{A}_j$, the text encoder $f_\lambda(\cdot)$ encodes the prompt to a text embedding. The embedding to represent the j -th defect state can be represented by

$$\mathbf{z}^{D_k} = \frac{1}{E} \sum_{\mathbf{P} \in \mathcal{A}_k} f_\lambda(\mathbf{P}), k \in \{1, \dots, K\} \quad (5)$$

Similarly, the embedding for the normal state is

$$\mathbf{z}^N = \frac{1}{E} \sum_{\mathbf{P} \in \mathcal{B}} f_\lambda(\mathbf{P}). \quad (6)$$

In total, we have $K+1$ embeddings $\{\mathbf{z}^N, \mathbf{z}^{D_1}, \dots, \mathbf{z}^{D_K}\}$ represent one normal state and K abnormal state.

4.3. Loss Function Design

Our loss function consists of two components: The global loss uses cosine similarity to align the global image embedding with its corresponding normal or abnormal state, capturing high-level semantic differences between samples. This is achieved by calculating the cosine similarity between the global image embedding \mathbf{z}^x with \mathbf{z}^N and the averaged defect-aware prompts, $\frac{1}{K} \sum_{j=1}^K \mathbf{z}^{D_k}$ to get the similarity score $\mathbf{s} \in \mathbb{R}^2$. The global loss is defined by

$$\mathcal{L}_{\text{global}} = CE(\text{softmax}(\mathbf{s}), y), \quad (7)$$

where $CE(\cdot)$ represents the cross-entropy calculation.

The local loss aligns image patch embeddings with one of the $K+1$ states at a fine-grained spatial resolution. Each adapted image patch embeddings \mathbf{Z}_i^p is compared with

$K+1$ text embeddings to get the similarity map. Since we choose image patch embeddings at M different layers, we get M different similarity maps $\hat{\mathbf{S}}_i \in \mathbb{R}^{(K+1) \times H' \times W'}$. This allows the model to localize and differentiate between defect types and normal regions at a finer spatial resolution. The local loss is defined by:

$$\begin{aligned} \mathcal{L}_{\text{local}} = & \frac{1}{M} \sum_{i=1}^M Focal(UP(\hat{\mathbf{S}}_i), \mathbf{Y}) + Dice(UP(\hat{\mathbf{S}}_i[0]), \mathbf{Y}[0]) \\ & + Dice(\mathbf{1} - UP(\hat{\mathbf{S}}_i[0]), \mathbf{1} - \mathbf{Y}[0]), \end{aligned} \quad (8)$$

where $Focal(\cdot)$, and $Dice(\cdot)$ are focal [23] and dice [21] losses, respectively. Focal loss is designed to address the class imbalance problem, which is especially relevant in AD, where anomalous samples are significantly fewer than normal ones. Dice loss encourages the model to learn accurate decision boundaries by measuring the overlap between the predicted and ground truth segmentation mask. $UP(\cdot)$ is the upsampling function to enlarge the resolution to the original image size $H \times W$. $\hat{\mathbf{S}}_i[0]$ represents the predicted probability map for the normal state at stage i . $\mathbf{Y} \in \mathbb{R}^{(K+1) \times H \times W}$ represents the ground truth of the multi-defect type segmentation and $\mathbf{Y}[0]$ is the layer for the normal part. The final loss is a weighted combination of the global and local losses:

$$\mathcal{L}_{\text{total}} = \mathcal{L}_{\text{global}} + \lambda \mathcal{L}_{\text{local}} \quad (9)$$

where λ is a hyperparameter used for balancing.

It is important to note that the underlying feature spaces of both text and vision modalities are pre-trained to capture image-text semantics, rather than anomaly semantics. This motivates refining the embedding space to better align the modalities within the anomaly detection domain, as described in the following section.

4.4. Progressive Fine Tuning

To better align the textual and visual modalities, we adapt prefix tuning [14, 22] to refine CLIP's representation by inserting learnable tokens into both the text and vision transformers. Specifically, we leverage progressive-VPT [32] to both modalities using a progressive connection mechanism. For the text encoder, we introduce at the prefix part of the original token embeddings and progressively refine them across layers. At each transformer layer, a new set of learnable tokens is connected rather than completely replacing the old ones. This allows the gradual adaptation of the text representation towards defect-aware semantics. This process is repeated until the designated depth N_d is reached. Similarly, for the vision encoders, we apply progressive visual prompt tuning, where learnable tokens are gradually introduced at each layer.

Formally, T_j represents the input tokens and U_j represents the learnable tokens introduced at the j -th layer. The output token at each transformer layer is computed as:

$$[T_j, O_j] = \begin{cases} f_j([T_0, U_1]), & \text{if } j = 1 \\ f_j([T_{j-1}, (1-\alpha)U_j + \alpha O_{j-1}]), & \text{otherwise} \end{cases} \quad (10)$$

where $\alpha \ll 1$ is a small decaying parameter that controls the contribution of the previous layer output. f_j is the function at encoder layer j .

4.5. Training and Inference

During each training iteration, the vision encoder processes the input images to produce a global image embedding $\mathbf{z}^x \in \mathcal{Z}$ and intermediate patch embeddings from M different encoding layers. Each linear adapter from M stages projects the patch embeddings into the shared vision-text space \mathcal{Z} , resulting in adapted patch embeddings $\mathbf{Z}_i^p \in \mathbb{R}^{C \times H' \times W'}$. The text encoder processes the $K + 1$ set of learnable prompts to produce the corresponding text embeddings $\mathbf{z}^t \in \mathcal{Z}$. The global image embedding and the adapted patch embeddings are then aligned with the text embedding using the loss function λ_{total} defined in 9. The adapted patch embeddings are used to compute similarity maps through normalized dot products with $K + 1$ text embedding $\hat{\mathbf{S}}_i \in \mathbb{R}^{(K+1) \times H' \times W'}$. These similarity maps are then up-sampled using an interpolation operation $UP(\cdot)$ to match the input image resolution $\hat{\mathbf{S}}_i \in \mathbb{R}^{(K+1) \times H \times W}$ for alignment with the ground-truth segmentation masks. During backpropagation, only the learnable tokens and M linear adapter layers are updated. The pre-trained text and vision encoders remain frozen throughout the training.

During inference, images from the target dataset are processed using the same forward pass pipeline as in training, but without gradient computation. For a given image, the model generates adapted patch embeddings from M stages and a set of $K' + 1$ text embeddings corresponding to the ‘normal’ class and the K' defect types relevant to the target object. The inference procedure then diverges depending on the desired task. For binary AD, the goal is to produce a single anomaly score for each pixel. This is achieved by focusing only on the similarity map corresponding to the ‘normal’ class, $\hat{\mathbf{S}}[0]$. The final anomaly map is obtained by inverting these normal predictions: $UP(1 - \hat{\mathbf{S}}[0])$. This creates a heatmap where regions with a low probability of being normal are highlighted as anomalous. For multi-type AS, the full set of similarity maps is utilized. A pixel-wise similarity calculation is performed between the adapted patch embeddings and the set of all $K' + 1$ text embeddings. This results in a multi-channel similarity map for each of the M stages, where each channel corresponds to the likelihood of a specific defect type. The similarity maps

from each of the M stages are then element-wise summed to produce a final, aggregated prediction map. This map, with dimensions $(K' + 1) \times H' \times W'$, contains the combined evidence for each defect class at every pixel location. From this multi-channel map, a final segmentation can be obtained by applying a pixel-wise argmax operation, which assigns each pixel to the defect category with the highest similarity score. This produces a final integer mask where each value corresponds to a specific defect class.

5. Experiments

In this section, we describe the experimental setup, datasets, and evaluation metrics, and discuss the results.

5.1. Datasets

We evaluated DAPO on five public datasets: MVTec-AD [1], VisA [45], MPDD [12], MAD [40], Real-IAD [31], and an internal dataset.

5.2. Implementation Details

We adopt the CLIP-OpenCLIP [10], specifically the available VIT-L/14@336 model pretrained on OpenAI. The parameters of both text and vision encoders in CLIP are kept frozen throughout the experiment. The learnable tokens are attached to all the transformer layers, with 4 learnable tokens per layer. The length of the learnable prompt l is set to 5 for both normal and abnormal prompts by setting the number of prompts E as 10. We finetune DAPO using the test set of the MVTec-AD and tested it on other target datasets. λ is set to 4.0, with input images resized to 518×518 , and a batch size of 8. More details are in the Appendix.

5.3. Evaluation Metrics

To evaluate the performance of our approach, we use the area under the receiver operating characteristic curve (AUROC), average precision (AP) for anomaly detection. For segmentation, we use pixel-level AUROC and the area under per-region overlap (AUPRO). For multi-type segmentation, we use AUROC, AP, and F1 by macro-averaging.

6. Results

We evaluate our approach on two primary tasks: (1) Binary AD/AS under distribution shift. (2) Multi-Type AS, a novel task to evaluate fine-grained localization.

6.1. Multi-type Anomaly Segmentation

We first evaluate our primary contribution: using prompt-learning for zero-shot multi-type AS. We compare our method with the handcrafted prompt baseline, MultiTADS [28]. The performance comparison is detailed in Table 1. To the best of our knowledge, we are the first to use a prompt learning approach for the multi-type AS

Table 1. Zero-Shot Multi-type Anomaly Segmentation performance. Best results are highlighted in bold. MultiADS results are directly reported from the original paper.

Dataset		Method	Pixel-Level		
Train	Test		AUROC	AP	F1-score
MVTec-AD	VisA	MultiADS	93.6	24.8	22.3
		DAPO (ours)	88.9	25.0	22.2
	MPDD	MultiADS	95.2	53	42.8
		DAPO (ours)	95.5	53.6	50.0
	MAD-Sim	MultiADS	92.1	31.5	27.9
		DAPO (ours)	91.9	33.3	25.0
	MAD-Real	MultiADS	89.2	52.3	52.5
		DAPO (ours)	86.1	58.5	58.5

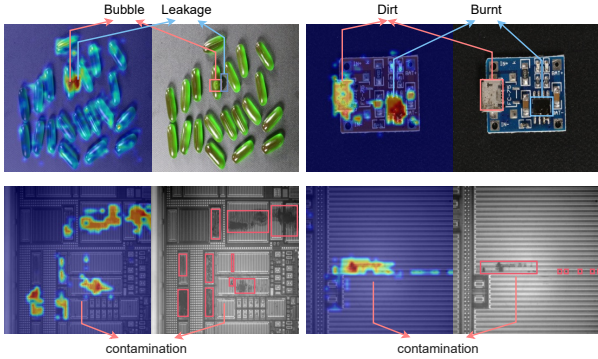


Figure 3. Anomaly segmentation results from DAPO on VisA, MVTec-AD, and the internal dataset. Top: unseen multi-defect cases (PCB, Capsules). Bottom: illustration of the contamination defect in the internal semiconductor dataset.

task. Our approach consistently outperforms MultiADS, measured by the AP metric, and achieves comparable or superior pixel-level F1 scores. The performance margin is the largest in MPDD with a +7.2% on F1-score and a +6.0% on MAD-Real datasets. This shows the strength of our prompt learning approach for localizing anomalies that are visually present, such as “scratches” or “cracks”. However, our method shows a slight decrease in the VisA and MAD-Sim dataset with respect to the AUROC metric. This performance trade-off is explained by the composition of the datasets. The lower AUROC on VisA and MAD-Real stems from the high frequency of “missing” component anomalies, which require object-level semantic priors to identify. Our method is not guided by such class semantics, while MultiADS uses class names to gain an advantage on these specific “absence” defects. In contrast, the superior AP and F1 scores demonstrate that for visually present anomalies, our defect-aware prompts improves the alignment between the modalities, leading to more accurate localization.

6.2. Per-defect Anomaly segmentation

To better understand the model’s generalization capabilities, we analyze its behavior on selected individual defect types

Table 2. Pixel-level segmentation results for representative seen and unseen defect types* across datasets. A complete list is provided in the Appendix.

Dataset	Defect	MultiADS		DAPO (ours)	
		AUROC	F1	AUROC	F1
VisA	Extra*	94.1	2.1	95.4	3.5
	Missing*	88.5	5.3	87.6	13.3
	Particle*	97.2	0.2	99.0	3.1
	Breakage*	98.5	7.9	97.1	20.8
MPDD	Flattening*	96.7	36.1	98.8	66.6
	Mismatch*	88.4	2.6	93.7	17.9
	Rust*	88.4	26.1	90.1	28.4
	Scratch	96.7	27.0	97.4	26.8
MAD-Real	Stains	97.0	6.1	98.7	40.4
	Missing	84.1	3.7	77.7	1.8
MAD-Sim	Burrs*	95.6	1.2	95.4	1.4
	Stains	98.2	15.0	99.2	30.0

(Table 2). The model demonstrates its ability to generalize to an extend to unseen(*) defect types that have a strong, visually-present signal, such as textural or geometric deviations. This is the primary reason for its improved performance on datasets like MPDD, where it achieves a F1-score of 66.6% on an unseen “flattening” defect. Similarly, for MAD-Real and VisA it effectively identifies “stains” with 40.4% F1-score compared to the baseline 6.1%, and 20.8% F1 for “breakage” compared to the baseline 7.8%, respectively. However, this strength is contrasted when handling anomalies that lack a strong, local visual signal. This limitation manifests in two ways. First, for fine-grained defects like “particles” on VisA, the model achieves a high detection (99% AUROC) but a very low segmentation precision (low F1). It recognizes that something is wrong but struggles to precisely localize the fine-grained anomalous region. Second, the model consistently struggles with defects defined by “missing” components. The results for the “missing” defect type (e.g., 1.8% F1 on MAD-Real) directly explain the overall AUROC gap we observed in Table 1. We believe that this primary weakness is rooted in the models patch-based architecture. A “missing” component leaves behind a visually normal patch (e.g., the background), which provides no anomalous signal for the ViT encoder to capture or align with a text prompt. This explains the performance gap we observed, while its strength in localizing certain visual anomalies. A clear direction for future work would be in integrating object-level priors, such as memory or few-shot techniques, to better reason about these discrepancies.

6.3. Binary Detection and Segmentation under Distribution Shift

Table 3 shows the performance of anomaly detection under distribution shift for pixel and image levels. Following baselines [28, 41], we train our model on MVTec-AD and test it on VisA, MPDD, and Real-IAD datasets. Our

Table 3. Binary anomaly detection and anomaly segmentation performance under distribution shift. Best results are in **bold**.

Binary AD & AS		Image-Level		Pixel-Level	
Dataset	Method	AUROC	AP	AUROC	AUPRO
VisA	CLIP-AC	65.0	70.1	24.8	17.3
	CoCoOp	78.1	-	93.6	-
	WinCLIP	78.1	81.2	79.6	56.8
	AprilGAN	78.0	81.4	94.2	86.8
	AnomalyCLIP	82.1	85.4	95.5	87.0
	AdaCLIP	75.4	79.3	95	-
	MultiADS	83.6	86.9	95	89.7
MPDD	DAPO (ours)	84.9	87.1	94.3	84
	CLIP-AC	56.2	66.0	58.7	29.1
	CoCoOp	61	-	95.1	-
	WinCLIP	63.6	69.9	76.4	48.9
	AprilGAN	73.0	80.2	94.1	83.2
	AnomalyCLIP	77.0	82.0	96.5	88.7
	AdaCLIP	66.3	75	96.3	-
Real-IAD	MultiADS	78.3	78.4	95.8	89.7
	DAPO (ours)	81.2	83.6	95.1	84.4
	WinCLIP	75	72.3	87.1	59.9
	AprilGAN	75.7	73.5	96	86.8
	AnomalyCLIP	78.4	76.7	96.2	85.7
	AdaCLIP	70.1	68.5	95.3	-
	MultiADS	78.7	79.1	96.6	87.1
	DAPO (ours)	84.3	84	96.4	80.3

Table 4. Binary anomaly detection performance under distribution shift on our internal semiconductor dataset.

Binary Anomaly Detection		Image-Level	
Dataset	Method	AUROC	AP
Semi-conductor (Internal Dataset)	AnomalyCLIP	68.2	35.3
	MultiADS	91.1	61.7
DAPO (ours)		91.8	79.1

method achieves the best image-level anomaly detection performance across all datasets, with the highest AUROC and AP scores, demonstrating strong generalization under distribution shift. Our pixel-level results are competitive, though AUPRO trails to the baselines. The experiments of our internal dataset (Table 4) suggests that AnomalyCLIP might be overfitting to public benchmarks, as it performs significantly worse compared to other methods, achieving only 68.2 AUROC score and 35.3 AP score, indicating poor generalization under distribution shift (cf. 3). The performance drop of AnomalyCLIP highlights the importance of semantic defect type information for improved generalization, as shown by both MultiADS and our approach.

Also, we evaluated our internal dataset using a confusion matrix at threshold 0.5 and a ROC curve as shown in Figure 4. Unlike AnomalyCLIP, which misclassified all samples as anomalies, our model showed balanced classification, demonstrating robust performance.

6.4. Ablation Study

We study the effect of regularization term λ and prompt length l . Figure 8(a) shows that penalizing the multi-class

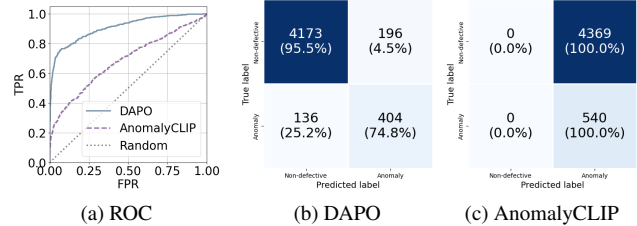


Figure 4. Binary anomaly detection performance comparison. (a) ROC curves for DAPO, AnomalyCLIP, and Random Classifier. (b) and (c) are confusion matrices, demonstrating classification accuracy, with our approach, DAPO, achieving the best overall performance compared to AnomalyCLIP.

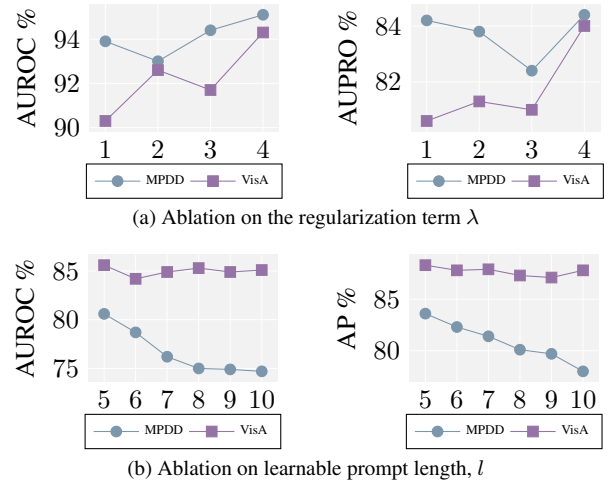


Figure 5. Hyperparameter analysis. a) weight balance λ , b) length l . Pixel-(top) and Image-(bottom)-level AUROC and AUPRO/AP are shown on the left and right of each subplot.

segmentation by increasing λ initially improves detection, followed by a slight drop and recovery. We observe in Figure 8(b) that longer prompts reduce performance, likely due to overfitting on the training dataset. See the appendix for more ablation studies.

7. Conclusion

We introduced DAPO, a prompt-based method for multi-defect and binary anomaly detection and segmentation. DAPO uses a shared set of learnable contextual tokens combined with defect-specific terms to shift representations into appropriate semantic spaces, eliminating the need for manually crafted prompts. We apply progressive tuning across text and image spaces, enabling effective task adaptation. Experiments on five public benchmarks and an internal industrial dataset show that DAPO achieves strong performance, particularly under distribution shifts.

References

[1] Paul Bergmann, Michael Fauser, David Sattlegger, and Carsten Steger. Mvtec ad—a comprehensive real-world dataset for unsupervised anomaly detection. In *Proceedings of the IEEE/CVF conference on computer vision and pattern recognition*, pages 9592–9600, 2019. 6, 1

[2] Yunkang Cao, Jiangning Zhang, Luca Frittoli, Yuqi Cheng, Weiming Shen, and Giacomo Boracchi. Adaclip: Adapting clip with hybrid learnable prompts for zero-shot anomaly detection. In *European Conference on Computer Vision*, pages 55–72. Springer, 2024. 2, 1, 4

[3] Xuhai Chen, Yue Han, and Jiangning Zhang. April-gan: A zero-/few-shot anomaly classification and segmentation method for cvpr 2023 vand workshop challenge tracks 1&2: 1st place on zero-shot ad and 4th place on few-shot ad. *arXiv preprint arXiv:2305.17382*, 2023. 2, 1

[4] N Cohen and Y Hoshen. Sub-image anomaly detection with deep pyramid correspondences. arxiv 2020. *arXiv preprint arXiv:2005.02357*, 2005. 2

[5] Thomas Defard, Aleksandr Setkov, Angelique Loesch, and Romaric Audigier. Padim: a patch distribution modeling framework for anomaly detection and localization. In *International conference on pattern recognition*, pages 475–489. Springer, 2021. 1, 2

[6] Chenghao Deng, Haote Xu, Xiaolu Chen, Haodi Xu, Xiaotong Tu, Xinghao Ding, and Yue Huang. Simclip: Refining image-text alignment with simple prompts for zero-/few-shot anomaly detection. In *Proceedings of the 32nd ACM International Conference on Multimedia*, pages 1761–1770, 2024. 2

[7] Hanqiu Deng and Xingyu Li. Anomaly detection via reverse distillation from one-class embedding. In *Proceedings of the IEEE/CVF conference on computer vision and pattern recognition*, pages 9737–9746, 2022. 1, 2

[8] Ian Goodfellow, Jean Pouget-Abadie, Mehdi Mirza, Bing Xu, David Warde-Farley, Sherjil Ozair, Aaron Courville, and Yoshua Bengio. Generative adversarial networks. *Communications of the ACM*, 63(11):139–144, 2020. 2

[9] Zhaopeng Gu, Bingke Zhu, Guibo Zhu, Yingying Chen, Hao Li, Ming Tang, and Jinqiao Wang. Filo: Zero-shot anomaly detection by fine-grained description and high-quality localization. In *Proceedings of the 32nd ACM International Conference on Multimedia*, pages 2041–2049, 2024. 2

[10] Gabriel Ilharco, Mitchell Wortsman, Ross Wightman, Cade Gordon, Nicholas Carlini, Rohan Taori, Achal Dave, Vaishaal Shankar, Hongseok Namkoong, John Miller, et al. Openclip. *If you use this software, please cite it as below*, 7, 2021. 6

[11] Jongheon Jeong, Yang Zou, Taewan Kim, Dongqing Zhang, Avinash Ravichandran, and Onkar Dabeer. Winclip: Zero-/few-shot anomaly classification and segmentation. In *Proceedings of the IEEE/CVF Conference on Computer Vision and Pattern Recognition*, pages 19606–19616, 2023. 2, 1

[12] Stepan Jezek, Martin Jonak, Radim Burget, Pavel Dvorak, and Milos Skotak. Deep learning-based defect detection of metal parts: evaluating current methods in complex conditions. In *2021 13th International congress on ultra modern telecommunications and control systems and workshops (ICUMT)*, pages 66–71. IEEE, 2021. 6, 1

[13] Zhengbao Jiang, Frank F Xu, Jun Araki, and Graham Neubig. How can we know what language models know? *Transactions of the Association for Computational Linguistics*, 8: 423–438, 2020. 2

[14] Muhammad Uzair Khattak, Hanoona Rasheed, Muhammad Maaz, Salman Khan, and Fahad Shahbaz Khan. Maple: Multi-modal prompt learning. In *Proceedings of the IEEE/CVF conference on computer vision and pattern recognition*, pages 19113–19122, 2023. 5

[15] Diederik P Kingma and Jimmy Ba. Adam: A method for stochastic optimization. *arXiv preprint arXiv:1412.6980*, 2014. 2

[16] Diederik P Kingma, Max Welling, et al. Auto-encoding variational bayes, 2013. 2

[17] Alexander Kirillov, Eric Mintun, Nikhila Ravi, Hanzi Mao, Chloe Rolland, Laura Gustafson, Tete Xiao, Spencer Whitehead, Alexander C Berg, Wan-Yen Lo, et al. Segment anything. In *Proceedings of the IEEE/CVF international conference on computer vision*, pages 4015–4026, 2023. 2

[18] Yann LeCun et al. Generalization and network design strategies. *Connectionism in perspective*, 19(143-155):18, 1989. 2

[19] Brian Lester, Rami Al-Rfou, and Noah Constant. The power of scale for parameter-efficient prompt tuning. *arXiv preprint arXiv:2104.08691*, 2021. 2

[20] Shengze Li, Jianjian Cao, Peng Ye, Yuhan Ding, Chongjun Tu, and Tao Chen. Clipsam: Clip and sam collaboration for zero-shot anomaly segmentation. *Neurocomputing*, 618: 129122, 2025. 2

[21] Xiaoya Li, Xiaofei Sun, Yuxian Meng, Junjun Liang, Fei Wu, and Jiwei Li. Dice loss for data-imbalanced nlp tasks. *arXiv preprint arXiv:1911.02855*, 2019. 5

[22] Xiang Lisa Li and Percy Liang. Prefix-tuning: Optimizing continuous prompts for generation. *arXiv preprint arXiv:2101.00190*, 2021. 5

[23] Tsung-Yi Lin, Priya Goyal, Ross Girshick, Kaiming He, and Piotr Dollár. Focal loss for dense object detection. In *Proceedings of the IEEE international conference on computer vision*, pages 2980–2988, 2017. 5

[24] Yunfei Liu, Chaoqun Zhuang, and Feng Lu. Unsupervised two-stage anomaly detection. *arXiv preprint arXiv:2103.11671*, 2021. 2

[25] Laurens van der Maaten and Geoffrey Hinton. Visualizing data using t-sne. *Journal of machine learning research*, 9 (Nov):2579–2605, 2008. 3

[26] Alec Radford, Jong Wook Kim, Chris Hallacy, Aditya Ramesh, Gabriel Goh, Sandhini Agarwal, Girish Sastry, Amanda Askell, Pamela Mishkin, Jack Clark, et al. Learning transferable visual models from natural language supervision. In *International conference on machine learning*, pages 8748–8763. PMLR, 2021. 1

[27] Karsten Roth, Latha Pemula, Joaquin Zepeda, Bernhard Schölkopf, Thomas Brox, and Peter Gehler. Towards total recall in industrial anomaly detection. In *Proceedings of the IEEE/CVF conference on computer vision and pattern recognition*, pages 14318–14328, 2022. 1, 2

[28] Ylli Sadikaj, Hongkuan Zhou, Lavdim Halilaj, Stefan Schmid, Steffen Staab, and Claudia Plant. Multiads: Defect-aware supervision for multi-type anomaly detection and segmentation in zero-shot learning. *arXiv preprint arXiv:2504.06740*, 2025. 2, 3, 6, 7, 1, 4

[29] Simon Schrödi, David T Hoffmann, Max Argus, Volker Fischer, and Thomas Brox. Two effects, one trigger: on the modality gap, object bias, and information imbalance in contrastive vision-language representation learning. *arXiv preprint arXiv:2404.07983*, 2024. 2

[30] Shashanka Venkataraman, Kuan-Chuan Peng, Rajat Vikram Singh, and Abhijit Mahalanobis. Attention guided anomaly localization in images. In *European Conference on Computer Vision*, pages 485–503. Springer, 2020. 2

[31] Chengjie Wang, Wenbing Zhu, Bin-Bin Gao, Zhenye Gan, Jiangning Zhang, Zhihao Gu, Shuguang Qian, Mingang Chen, and Lizhuang Ma. Real-iad: A real-world multi-view dataset for benchmarking versatile industrial anomaly detection. In *Proceedings of the IEEE/CVF Conference on Computer Vision and Pattern Recognition*, pages 22883–22892, 2024. 6, 1

[32] Chen Xu, Yuhua Zhu, Haocheng Shen, Boheng Chen, Yixuan Liao, Xiaoxin Chen, and Limin Wang. Progressive visual prompt learning with contrastive feature re-formation. *International Journal of Computer Vision*, 133(2):511–526, 2025. 5

[33] Jie Yang, Yong Shi, and Zhiqian Qi. Dfr: Deep feature reconstruction for unsupervised anomaly segmentation. *arXiv preprint arXiv:2012.07122*, 2020. 1, 2

[34] Xiangtong Yao, Tobias Blei, Yuan Meng, Yu Zhang, Hongkuan Zhou, Zhenshan Bing, Kai Huang, Fuchun Sun, and Alois Knoll. Long-horizon language-conditioned imitation learning for robotic manipulation. *IEEE/ASME Transactions on Mechatronics*, pages 1–12, 2025. 2

[35] Hongkuan Zhou, Xiangtong Yao, Oier Mees, Yuan Meng, Ted Xiao, Yonatan Bisk, Jean Oh, Edward Johns, Mohit Shridhar, Dhruv Shah, Jesse Thomason, Kai Huang, Joyce Chai, Zhenshan Bing, and Alois Knoll. Bridging language and action: A survey of language-conditioned robot manipulation. *CoRR*, abs/2312.10807, 2023.

[36] Hongkuan Zhou, Zhenshan Bing, Xiangtong Yao, Xiaojie Su, Chenguang Yang, Kai Huang, and Alois Knoll. Language-conditioned imitation learning with base skill priors under unstructured data. *IEEE Robotics and Automation Letters*, 9(11):9805–9812, 2024. 2

[37] Hongkuan Zhou, Stefan Schmid, Yicong Li, Lavdim Halilaj, Xiangtong Yao, and Wei Cao. Predicting the road ahead: A knowledge graph based foundation model for scene understanding in autonomous driving. In *The Semantic Web*, pages 116–132, Cham, 2025. Springer Nature Switzerland. 2

[38] Kaiyang Zhou, Jingkang Yang, Chen Change Loy, and Ziwei Liu. Conditional prompt learning for vision-language models. In *Proceedings of the IEEE/CVF conference on computer vision and pattern recognition*, pages 16816–16825, 2022. 2, 1

[39] Kaiyang Zhou, Jingkang Yang, Chen Change Loy, and Ziwei Liu. Learning to prompt for vision-language models. *International Journal of Computer Vision*, 130(9):2337–2348, 2022. 2, 1

[40] Qiang Zhou, Weize Li, Lihan Jiang, Guoliang Wang, Guyue Zhou, Shanghang Zhang, and Hao Zhao. Pad: A dataset and benchmark for pose-agnostic anomaly detection. *Advances in Neural Information Processing Systems*, 36:44558–44571, 2023. 6, 1

[41] Qihang Zhou, Guansong Pang, Yu Tian, Shibo He, and Jiming Chen. Anomalyclip: Object-agnostic prompt learning for zero-shot anomaly detection. *arXiv preprint arXiv:2310.18961*, 2023. 2, 4, 7, 1

[42] Xingcheng Zhou, Mingyu Liu, Ekim Yurtsever, Bare Luka Zagar, Walter Zimmer, Hu Cao, and Alois C. Knoll. Vision language models in autonomous driving: A survey and outlook. *IEEE Transactions on Intelligent Vehicles*, pages 1–20, 2024. 2

[43] Jiawen Zhu, Yew-Soon Ong, Chunhua Shen, and Guansong Pang. Fine-grained abnormality prompt learning for zero-shot anomaly detection. *arXiv preprint arXiv:2410.10289*, 2024. 3

[44] Mohammad Zolfaghari and Hedieh Sajedi. Unsupervised anomaly detection with an enhanced teacher for student-teacher feature pyramid matching. In *2022 27th International Computer Conference, Computer Society of Iran (CSC-ICC)*, pages 1–4. IEEE, 2022. 1, 2

[45] Yang Zou, Jongheon Jeong, Latha Pemula, Dongqing Zhang, and Onkar Dabeer. Spot-the-difference self-supervised pre-training for anomaly detection and segmentation. In *European Conference on Computer Vision*, pages 392–408. Springer, 2022. 6, 1

Defect-aware Hybrid Prompt Optimization via Progressive Tuning for Zero-Shot Multi-type Anomaly Detection and Segmentation

Supplementary Material

In the appendix, we discuss the key statistics of the five publicly available datasets and one internal dataset. Additionally, the baselines we compared are briefly described. Finally, additional experiments with detailed results, along with visualizations, are listed.

8. Datasets

In this section, we describe the public benchmark industrial datasets, MvTec-AD [1], VisA [45], MPDD [12], MAD [40], Real-IAD [31], along with an internal dataset. Table 5 summarizes key statistics of these datasets, including the number of distinct product classes and the distribution of normal and anomalous samples. Each product may exhibit multiple defect types, which are categorized into their respective defect classes as introduced in Multi-ADS [28]. More detailed defect-level descriptions for each dataset can be found in the supplementary material of the original MultiADS paper. Our internal dataset consists of high-resolution semiconductor chip images collected from an industrial environment, featuring a single known defect type. It provides realistic, real-world conditions for evaluating the robustness of the proposed system under distribution shift. For our internal dataset, only bounding box annotations were available for the segmentation task, which were used to generate corresponding anomaly masks. Hence, the pixel-level scores are not accurate for evaluating the localization performance. The details of the defect types are mentioned in the Table 5.

Table 5. Key statistics of the datasets used for industrial anomaly detection.

Dataset	$ C $	#Normal / #Anomalous	Usage
MVTec AD	15	(467; 1258)	Industrial defect detection
VisA	12	(962; 1200)	Industrial defect detection
MPDD	6	(176; 282)	Industrial defect detection
MAD	20	(5,231; 4902)	Simulated defect detection
Real-IAD	30	(99,721; 51,326)	Industrial defect detection
Semi-conductor (internal dataset)	1	(4,369; 540)	Industrial defect detection

9. Baselines

To evaluate the performance of our DAPO, we compare DAPO with several baseline models. The results of the

baselines are taken directly from the respective papers. Details of the respective baselines are given as follows:

- **CLIP-AC** [26]: They use an ensemble of text prompts designed for normal and abnormal classes, e.g., *a photo of a normal [cls]*, and *a photo of a damaged [cls]*, where *[cls]* denotes the target class name. The generated embeddings are averaged to represent the normal and abnormal classes respectively. The anomaly scores are computed using the contrastive equation from [26]. Results are taken from [28]. For anomaly segmentation, the similarity score checking is extended to local embeddings extracted from patch features.
- **WinClip** [11]: WinClip is the primary baseline for anomaly detection under distribution shift. It uses a set of handcrafted prompts specific to the anomaly detection domain. For segmentation, a window-based approach is used due to the inherent limitation of pre-trained CLIP. The results are directly taken from the [28] paper.
- **AprilGAN** [3]: This approach extends the WinClip by introducing an additional linear adapter to achieve better accurate segmentation results. The results are taken directly from the [28].
- **CoCoOp** [38]: CoCoOp extend the CoOp [39]. To adapt CoOp for anomaly detection, authors of [41] extends the learnable text prompt templates $[V_1][V_2] \dots [V_n][\text{cls}]$ with $[V_1][V_2] \dots [V_n][\text{anomaly}][\text{cls}]$. Due to the sensitivity of the class distribution shift, CocoOp builds a light neural network to generate an instance conditional embeddings that adapts the learned prompts to the respective test set domains. The results are directly taken from the paper [28].
- **AnomalyCLIP** [41]: AnomalyCLIP is the primary prompt learning baseline for anomaly detection. They learn object-agnostic prompts that capture anomaly semantics. The learnable tokens are structured similarly to CoOp, but instead of including *[cls]* information, they use object-level semantics: $[V_1][V_2] \dots [V_n][\text{anomaly}][\text{object}]$, where *[object]* refers to the object as whole. The results are directly taken from their original paper [41].
- **AdaCLIP** [2]: AdaCLIP uses a hybrid prompt strategy combining static templates and dynamically generated prompts per test instance for CLIP adaptation. This hybrid design enables anomaly detection under distribution shifts. The results for AdaCLIP are directly taken from their original paper.
- **MultiADS** [28]: MultiADS is the key baseline for multi-

defect anomaly segmentation in zero-shot, and anomaly detection under distribution shifts. They use extensive prompt templates associated with each defect type and a product class. For e.g., *a photo of a [cls] having a [D] defect.* Here the *[cls]*, and *[D]* are replaced with class and defect information. The embeddings are then compared with the patch-level scores to generate local anomaly maps. The anomaly scores are computed by aggregating known anomaly scores. The results are directly from their paper.

10. Experiments

Here, we will discuss in detail on DAPO through the experiments, and the ablation we carried out. We will also display the visualization and fine-grained results of our approach.

10.1. Implementation Details

As mentioned in the “implementation details” subsection of main paper, we use **VIT-L/14@336** model pretrained on **OpenAI**. The model is optimized using Adam [15], with learning rate 0.001, and a batch size of 8. The number of intermediate patch-level features, M is 4, specifically from layers 6, 12, 18, 24. In line with prior works, we also follow a transfer learning strategy: training on Mvtec-AD and evaluating on other datasets, and train on VisA to test on Mvtec-AD. Input images are resized to 518 and normalized following the CLIP preprocessing pipeline. All our experiments are conducted for 5 epochs, with Pytorch-2.7.0, on a single NVIDIA-H200 GPU. Empirically, we found observed that performance peaks around epoch 1 or 2, with later epochs exhibiting overfitting to the training dataset.

10.2. Initialization of Prompts

We study the initialization strategy of the learnable tokens: normal context tokens V , abnormal context tokens W and layer tokens. We conducted experiments using three distinct initialization strategies: We used random initialization and found that the model achieved its best performance only in later epochs, suggesting the model required a longer duration to stabilize and find the objective minimum. Secondly, we initialized the context and layer tokens by aligning them to the mean (μ) and standard deviation (σ) of the CLIP’s token embeddings. We found that when initialized within CLIP’s feature space, the model converged much faster and yielded better overall results compared to the random strategy. Finally, in order to explicitly separate the feature space of normal and abnormal context tokens, we shifted the initialization of abnormal tokens by an offset 5σ from the mean of the CLIP space. We and found that this required more epochs to achieve its best image-level results. However, the pixel level accuracy over these epochs was lower compared with the non-offset approach. In Figure 6, we present the Image and Pixel level results on the VisA and

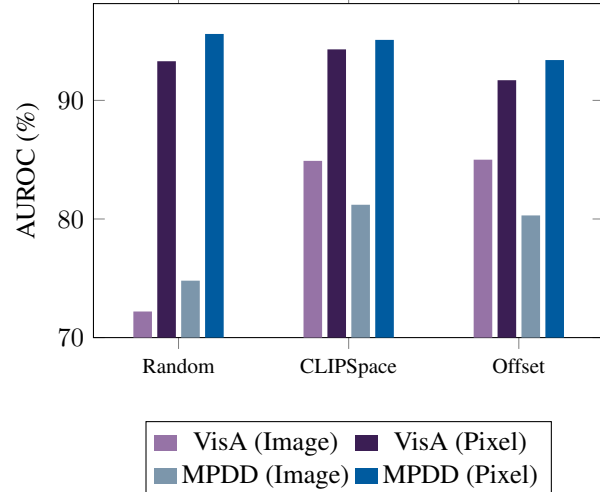


Figure 6. Performance comparison of token initialization strategies: **Random** ($\mathcal{N}(0, 1)$), **CLIP-Space** (aligned to CLIP’s μ, σ), and **Offset** (abnormal tokens shifted by 5σ). CLIP-Space provides faster convergence and higher pixel-level accuracy.

MPDD for each initialization strategy, using the best performing epoch achieved across 5 training cycles.

11. Prototype Aggregation

To determine the robust representation of the final anomaly prototype, z^{D_k} , We perform ablation on the aggregation method used to combine information from multiple defect prompts. Baseline: By default, we define the anomaly prototype prompt by calculating the simple average across all K defect-type prompts. This treated all defects equally, which can be noisy if only a few prompts are relevant to a specific image. Attention-weighted averaging: To filter out redundant or irrelevant prompts, we experimented with a weighted average based on the relevance of the prompt on the image. We calculated the attention weight w_i associated with each defect prompt embedding and the image embedding. The final prototype was then calculated as the weighted sum: $\frac{1}{K} \sum_{j=1}^K w_j * z^{D_k}$. We found that using an attention-weighted prototype did not yield significant performance improvement over the simple baseline mean. Both image, and pixel level scores showed only marginal gains or decrease in performance across the dataset, Table 6.

11.1. Prefix tuning approach

In this section, we demonstrate the effectiveness of the progressive tuning strategy compared to baseline prefix tuning. We train our model in MVTec-AD and evaluate it in MPDD. MPDD is selected for this evaluation due to its challenging conditions, including variable spatial orientations, diverse object positions and distances from the camera. The image-level AUROC and AP scores using progres-

Table 6. Prototype Aggregation Ablation: Simple Mean vs. Attention Weighting. The table display the Pixel and Image level AUROC scores on VisA and MPDD

Method	Dataset	Image(%)	Pixel (%)	Δ AP
Baseline	VisA	84.9	94.3	+3%
Attention	VisA	79.9	93.0	-3%
Baseline	MPDD	81.2	95.1	+3.2%
Attention	MPDD	78.0	91.9	-3.2%

Δ AP is the average change relative to the baseline for that dataset.

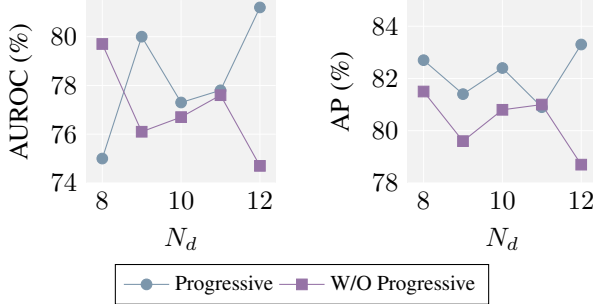


Figure 7. Ablation on the AUROC and AP with different N_d on MPDD using progressive and naive prefix tuning.

sive connection and traditional prefix tuning across different depths are shown in Figure 7. Detailed results of the best-performing configuration are provided in Table 7. We observe that with progressive connection, the model consistently achieves over 80% AP on MPDD, with minor fluctuations in AUROC, and clearly outperforms the traditional approach. These results highlight the importance of gradually adapting the encoders to better align image and text features, thereby improving anomaly detection performance across datasets. Here we keep the length of the learnable prompts, l as 5, and the number of learnable tokens as 4.

11.2. Prefix Depth

We study the impact of learnable tokens injection depth N_d on detection performance under distribution shift. The result shows that the relationship between N_d and detection performance is non-monotonic. Specifically, we observed an initial gain in performance followed by a small dip at intermediate depth, before reaching the maximum depth, Figure 8. This non-linear trend indicated that maximal integration is required for stability, as intermediate layers are highly sensitive. Therefore, for the final configuration, we utilized the full tested depth to have consistent performance. Please note that this ablation was performed only on the text encoder side of the architecture, as the visual prompt tuning was held constant at maximum layer depth (fully integrated into all visual transformer layers).

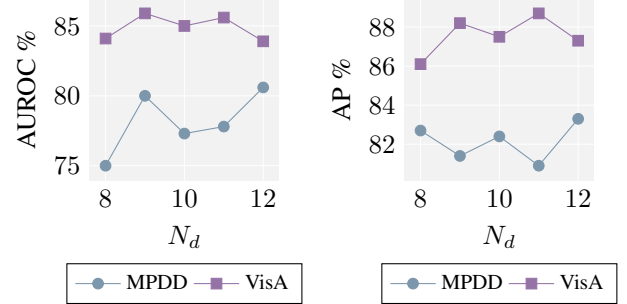


Figure 8. Effect on injecting learnable tokens at different depth of the text encoder.

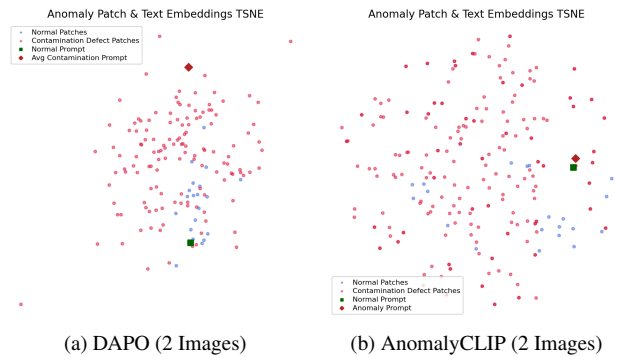


Figure 9. Comparison of feature topology. (a) Shows how patches are distributed and closer with the text-embedding in DAPO. (b) Shows how patches are scattered, with text embeddings in close proximity to each other in AnomalyCLIP.

11.3. Analysis of Feature Space

To visually verify the fine-grained feature topology of the learned embeddings, we utilized t-SNE [25] to project the high dimensional feature space into a 2D space. Our visualization comprises two distinct projections: a sample of 2 anomaly images (Figure 9 left) from DAPO, and the same sample of anomaly images (Figure 9 right) from AnomalyCLIP. In the projection, we observe a clear Euclidean separation between the normal and defect text anchor (“contamination” defect-type) in DAPO, as well as reasonable separation between anomaly (red) and normal (blue) patches, where normal patches are much closer towards the normal prompt. It shows that for individual samples, the model projects the normal and anomaly features into regions, creating a high local margin that facilitates better classification on instances. However, as in AnomalyCLIP, the topology shifts. The projection is scattered and the text anchors move into close proximity. This proximity treats defects as subtle perturbations of the normal classes, rather than as a separate disjoint domain. This could be the reason we believe that AnomalyCLIP was classifying every image as an anomaly in our internal dataset.

11.4. Additional Results

We demonstrate our model’s fine-grained, data-subset-level performance under distribution shifts. In Tables 8, we present the image-level and pixel-level results of our method, DAPO, evaluated on individual subsets of MPDD and VisA. These results are reported for anomaly detection under distribution shifts, a setting commonly referred to in the literature as zero-shot anomaly detection. Tables 9 present the results of our approach on the simulated datasets. We observe that our model consistently achieves the best or second-best performance at the image level, indicating its effectiveness in defect detection. It is important to note that both datasets contain numerous missing component anomalies, which contribute to the overall lower performance, particularly for MAD-Sim, which includes a significantly higher number of product images compared to MAD-Real. Table 10 shows the performance of our model on the Real-IAD dataset, a recent benchmark that contains approximately 20,000 test samples. Our method consistently achieves the best performance at the image level, demonstrating high AUROC and AP, even when compared to few-shot approaches such as MultiADS [28] and AdaCLIP [2], our method achieves near best performance as reported in the supplementary section of the MultiADS paper.

11.5. Internal Dataset

To evaluate our model’s robustness across varying thresholds in detecting anomalies on our internal semiconductor chip dataset, we plotted the False Positive Rate (FPR) and True Positive Rate (TPR) against different thresholds (see Figure 10). As illustrated, our model consistently outperforms the baseline AnomalyCLIP across all thresholds, demonstrating a stronger separation between the anomaly and normality spaces, and highlighting the discriminative power of our approach.

The consistent performance gap between our approach and AnomalyCLIP across all threshold values indicates the robustness of our progressive connection mechanism in handling distribution shifts inherent in real manufacturing environments. This stability is crucial for practical applications where threshold selection must balance detection sensitivity with operational efficiency. Furthermore, the smooth ROC curves demonstrate the reliability of our anomaly scoring mechanism, suggesting effective feature representations that capture anomaly patterns while maintaining discriminative power against normal variations in the manufacturing process.

11.6. Exploratory Study: Multi-label defect classification

While the primary focus of the work is binary anomaly detection and multi-type/binary anomaly segmentation, we

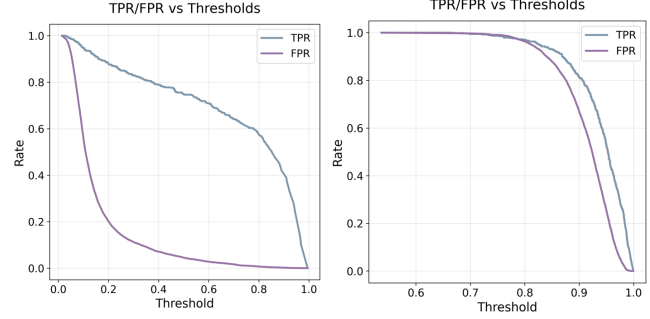


Figure 10. TPR and FPR across different threshold for anomaly detection under distribution shift. DAPO (ours) on Left, AnomalyCLIP on Right

extended our framework to explore **multi-label defect classification**. In this setting, we aim to identify the specific defect types present in an image (e.g., distinguishing between a *scratch*, *crack*, or *contamination*). Unlike standard multi-class classification which utilizes a Softmax distribution, real-world industrial defects are often non-exclusive. To address this, we treated the problem as a multi-label task. For a given image features, we computed the similarity logits with all potential defect text prompts and the normal prompt. To obtain independent probabilities for each defect type, we utilized a relative scoring mechanism. We subtracted the logit of the normal class from each defect class logit to center the scores around the decision boundary, followed by a Sigmoid activation:

$$P(D_k) = \sigma(\text{Sim}(z^x, z^{D_k}) - \text{Sim}(z^x, z^N)) \quad (11)$$

where σ is the sigmoid function. A defect D_k is predicted if $P(D_k) > 0.5$. We evaluated the Precision, Recall, and F1-Score (Macro-averaged) on the VisA and MPDD datasets. The results are presented in Table 11. The model exhibits high Recall (> 90% in many categories), indicating that defective images consistently trigger the defect prompts. Conversely, the Precision scores are consistently low (< 30%). This indicates a high rate of false positive predictions for specific defect classes. These results suggest that while the learnable tokens are effective at distinguishing *anomalous* samples from *normal* ones (driving the high Recall), they do not form mutually exclusive clusters for fine-grained defect types. The feature representations of similar defects remain entangled in the latent space, limiting the model’s ability to perform precise multi-type classification at the image level. However, for the downstream task of segmentation, this over-activation ensures that the pixel-level anomaly maps capture the defect region, regardless of the specific label ambiguity.

Table 7. Comparison of image-level performance on MPDD between progressive connection (DAPO) and without progressive connection, with overall mean per method.

Method	Bracket Black			Bracket Brown			Bracket White			Connector			Metal Plate			Tubes			Mean		
	AUROC	AP	F1	AUROC	AP	F1	AUROC	AP	F1	AUROC	AP	F1	AUROC	AP	F1	AUROC	AP	F1	AUROC	AP	F1
W/O Progressive	70.3	75.7	81.8	63.2	81.5	81.0	77.9	72.9	80.0	76.9	63.0	66.7	92.1	97.2	92.6	97.5	98.8	95.0	79.7	81.5	82.8
DAPO	73.6	78.9	81.5	59.6	77.3	80.6	85.4	83.1	81.7	75.2	65.0	63.4	96.1	98.7	93.5	97.0	98.8	95.5	81.2	83.6	82.7

11.7. Multi Type Anomaly Segmentation

We demonstrate our model’s ability to localize specific defect types, rather than merely detecting anomalies. In particular, we introduce a zero-shot setting, where defect types marked with (*) are unseen during training. This setting encourages future research on more generalized and robust defect segmentation. Table 12, 13, 14 present our model’s performance on the MAD (Simulated and Real), MPDD and VisA datasets, respectively. These results highlight the model’s effectiveness in segmenting both seen and unseen defect types.

12. Visualization

Here, we present the visualization of our anomaly segmentation results. We present six examples of object from VisA, MPDD, MVTec-AD, and Real-IAD datasets. Figures 11, 12, and 13 shows the capsule, fryum and pcb from VisA. Figures 15 and 16 shows the tubes and metal plate from MPDD dataset. Figures 17, 18, and 19 shows the Phone battery, sim card set, and fire wood from Real-IAD dataset. All visualizations illustrate segmentation results under distribution shift, where the model relies solely on prior knowledge of defect types available in the target set.

Table 8. **Binary Anomaly Detection and Segmentation:** Fine-grained performance on VisA and MPDD datasets.

VisA Dataset						MPDD Dataset					
Object	P-AUC	P-PRO	I-AUC	I-AP	I-F1	Object	P-AUC	P-PRO	I-AUC	I-AP	I-F1
Candle	98.3	91.5	89.3	91.9	82.0	Bracket Black	96.5	90.3	73.6	78.9	81.5
Capsules	96.6	73.1	86.3	92.5	84.4	Bracket Brown	91.1	74.4	59.6	77.3	80.6
Cashew	88.0	79.5	85.1	94.1	85.4	Bracket White	97.1	87.5	85.4	83.1	81.7
Chewinggum	99.5	89.5	95.9	98.4	95.3	Connector	94.7	82.9	75.2	65.0	63.4
Fryum	92.9	84.2	92.9	96.6	91.0	Metal Plate	92.1	75.3	96.1	98.7	93.5
Macaroni1	98.7	90.7	74.8	79.0	71.5	Tubes	99.0	96.1	97.0	98.8	95.5
Macaroni2	97.0	79.6	59.5	61.1	69.1						
PCB1	90.3	86.2	75.1	79.4	71.2						
PCB2	89.2	75.0	79.4	80.5	75.1						
PCB3	90.4	78.3	69.4	74.6	66.9						
PCB4	94.8	86.9	97.0	97.1	91.9						
Pipe Fryum	96.4	93.7	99.8	99.9	98.5						
Mean	94.3	84.0	83.7	87.1	81.9	Mean	95.1	84.4	81.2	83.6	82.7

Table 9. **Binary Anomaly Detection and Segmentation:** Fine-grained data-subset wise performance on MAD-Sim and MAD-Real datasets.

MAD-Sim Dataset						MAD-Real Dataset					
Object	P-AUC	P-PRO	I-AUC	I-AP	I-F1	Object	P-AUC	P-PRO	I-AUC	I-AP	I-F1
Elephant	67.6	57.9	61.2	91.7	94.0	Bear	99.7	98.6	79.2	95.0	94.1
Owl	90.0	65.6	54.9	89.4	93.0	Bird	78.0	40.3	54.5	85.5	89.8
Obesobeso	93.1	63.5	59.8	91.2	94.1	Elephant	78.0	47.6	78.9	93.7	88.9
Sabertooth	88.3	56.0	53.2	87.9	93.1	Parrot	60.7	40.1	75.7	95.1	90.2
Zalika	83.7	52.1	55.9	89.3	93.3	Pig	83.8	46.9	27.1	71.4	87.2
Mallard	85.2	50.0	58.1	93.7	95.6	Puppy	99.6	96.4	99.0	99.8	97.6
Bear	89.3	69.8	64.5	91.7	94.1	Scorpion	67.8	21.5	76.5	95.0	90.2
Cat	92.4	56.1	48.0	89.5	94.5	Turtle	99.6	97.0	100.0	100.0	100.0
Pig	93.3	61.6	60.0	91.7	94.0	Unicorn	83.1	52.8	68.6	91.1	89.4
Puppy	85.5	60.9	60.5	90.2	92.9	Whale	98.8	91.4	92.5	98.8	95.2
Parrot	81.8	65.4	54.7	87.2	91.8						
Pheonix	81.6	55.0	52.9	90.4	94.4						
Gorilla	91.2	61.2	60.4	94.3	96.0						
Unicorn	83.5	50.7	51.7	92.4	95.9						
Bird	89.9	47.8	55.9	92.0	94.4						
Swan	87.2	56.4	51.9	88.5	93.3						
Whale	87.7	69.5	53.9	89.6	94.4						
Scorpion	89.0	72.3	56.5	89.5	92.9						
Sheep	92.8	57.9	56.9	90.6	93.7						
Turtle	89.5	61.3	76.4	97.2	95.4						
Mean	87.1	59.5	57.4	90.9	94.0	Mean	84.9	63.3	75.2	92.6	92.3

Table 10. **Binary Anomaly Detection and Segmentation:** Fine-grained performance on Real-IAD dataset. The 30 object categories are split into two columns for efficient display.

Object	P-AUC	P-PRO	I-AUC	I-AP	I-F1	Object	P-AUC	P-PRO	I-AUC	I-AP	I-F1
Audiojack	97.3	79.5	62.2	55.1	52.5	U-Block	97.9	81.7	88.2	80.5	71.7
VCPill	98.7	89.4	90.6	88.2	78.9	Sim Card	99.5	93.7	96.0	97.3	92.7
Switch	85.6	71.1	81.3	90.2	80.7	Plastic Nut	95.3	67.2	84.4	64.7	56.4
USB Adaptor	94.4	57.0	76.8	73.2	69.5	Button Bat.	97.0	76.3	79.4	86.4	77.7
Eraser	99.2	86.5	87.0	87.6	79.7	Toothbrush	96.3	87.6	87.7	93.0	84.3
Fire Hood	99.1	93.7	95.8	90.4	85.1	Mounts	99.7	97.6	91.6	85.5	82.7
End Cap	93.7	72.0	68.1	75.4	75.5	Tape	99.6	94.9	98.5	98.0	92.7
Phone Bat.	98.4	83.4	89.1	91.9	84.9	Woodstick	99.1	90.5	88.3	74.2	67.9
Wood Beads	97.3	48.7	71.4	78.2	72.2	Bottle Cap	97.9	84.8	86.4	87.2	77.8
PCB	95.8	78.5	79.2	85.4	81.0	Porcelain	97.4	85.1	93.1	89.7	81.2
Mint	95.3	58.2	69.9	79.0	74.8	Toy Brick	98.8	86.6	84.7	83.9	75.0
Plastic Plug	98.3	85.9	88.4	88.1	79.1	Rolled Strip	99.2	93.8	94.3	97.4	91.3
Transistor	92.8	71.8	73.0	84.0	78.3	Terminal	97.8	84.6	94.4	96.8	91.6
Regulator	96.2	73.6	64.9	38.8	39.2	Zipper	93.0	83.6	97.5	99.0	95.8
Toy	82.6	62.9	77.3	88.7	81.2	USB	97.6	88.8	90.3	91.7	83.4
						Mean	96.4	80.3	84.3	84.0	77.8

Table 11. **Exploratory Image-Level Classification Results (Macro-Average %).** The high Recall vs. Low Precision trade-off indicates high sensitivity to anomalies but lower specificity for exact defect types.

VisA Dataset

MPDD Dataset

Category	Precision	Recall	F1-Score	Category	Precision	Recall	F1-Score
Candle	8.2	99.1	15.1	Bracket Black	36.0	94.3	49.5
Capsules	88.1	81.7	83.8	Bracket Brown	35.3	70.6	45.5
Cashew	16.6	76.1	26.6	Bracket White	27.4	100.0	43.0
Chewinggum	25.5	97.7	39.2	Connector	15.9	50.0	24.1
Fryum	18.4	71.1	28.6	Metal Plate	24.4	100.0	38.5
Macaroni1	11.5	99.3	20.2	Tubes	84.5	51.6	43.9
Macaroni2	8.8	100.0	15.5				
PCB1	13.1	80.3	21.6				
PCB2	13.1	98.5	22.2				
PCB3	12.0	100.0	21.1				
PCB4	5.2	100.0	9.5				
Pipe Fryum	19.5	99.3	32.0				

Table 12. **Multi-Type Segmentation:** Fine-grained data-subset wise results on MAD dataset.

MAD-Sim Dataset				MAD-Real Dataset			
Object	AUROC	F1	AP	Object	AUROC	F1	AP
Bear	93.7	25.0	37.6	Bear	98.7	62.3	60.6
Bird	94.2	25.0	27.9	Bird	80.8	49.8	51.0
Cat	94.9	25.0	27.0	Elephant	81.2	50.8	50.9
Elephant	81.7	24.9	33.1	Parrot	69.4	49.8	50.4
Gorilla	93.5	24.9	29.6	Pig	91.0	49.9	51.5
Mallard	91.4	24.9	36.8	Puppy	98.8	75.1	77.0
Obesobeso	94.7	25.0	27.2	Scorpion	65.0	49.6	50.6
Owl	93.4	24.9	34.6	Turtle	99.3	74.7	72.4
Parrot	89.3	25.0	34.9	Unicorn	78.7	49.9	50.3
Pheonix	87.6	24.9	25.9	Whale	98.0	72.4	70.8
Pig	95.4	24.9	32.3				
Puppy	90.7	25.1	44.3				
Sabertooth	93.2	24.9	30.5				
Scorpion	92.5	25.1	32.0				
Sheep	95.6	24.9	36.6				
Swan	92.2	24.9	27.6				
Turtle	94.3	25.0	39.5				
Unicorn	89.4	24.9	39.8				
Whale	92.1	25.3	38.0				
Zalika	88.8	24.9	31.6				
Mean	91.9	25.0	33.3	Mean	86.1	58.5	58.5

Table 13. **Multi-Type Segmentation on MPDD:** Detailed defect-wise and object-wise performance. (*) indicates defects unseen during training.

Defect-Wise Results			Object-Wise Results			
Defect Type	AUROC	F1	Object	AUROC	F1	AP
Good	95.66	99.86	Bracket black	97.1	37.9	35.9
Bent	90.37	2.85	Bracket brown	91.1	33.4	34.6
Defective painting*	93.22	0.06	Bracket white	97.0	38.5	37.0
Flattening*	98.79	66.57	Connector	95.2	68.2	67.4
Hole	98.62	1.14	Metal plate	93.7	41.6	63.5
Mismatch*	93.71	17.94	Tubes	98.8	80.2	83.3
Rust*	90.12	28.37				
Scratch	97.35	26.79				
Mean	95.5	50.0	53.6			

Table 14. **Multi-Type Segmentation on VisA:** Detailed defect-wise and object-wise performance. (*) indicates defects unseen during training.

Defect-Wise Results						Object-Wise Results			
Defect	AUC	F1	Defect	AUC	F1	Object	AUC	F1	AP
Normal	86.79	99.9	Melded	95.97	9.51	Candle	90.7	13.9	16.0
Bent	90.83	1.08	Melt	93.47	7.54	Capsules	77.0	54.8	50.9
Breakage	97.05	20.8	Missing	87.62	13.3	Cashew	89.6	18.4	25.0
Bubble	77.03	1.71	Particle	99.03	3.10	Chewinggum	96.7	27.2	42.4
Burnt	95.64	8.46	Scratch	89.73	1.89	Fryum	91.4	18.6	20.9
Chip	81.96	0.17	Spot	87.96	1.11	Macaroni1	88.2	20.0	20.1
Crack	83.75	0.14	Stuck	86.70	9.04	Macaroni2	77.8	16.7	16.7
Damage	93.24	1.63	Weird wick	79.04	0.05	PCB1	90.3	20.1	23.5
Extra	95.33	3.49	Wrong place	93.24	0.29	PCB2	88.6	20.1	21.7
Hole	95.24	1.49				PCB3	85.6	20.0	20.9
						PCB4	93.9	15.7	16.2
						Pipe fryum	97.0	20.9	26.3
						Mean	88.9	22.2	25.0

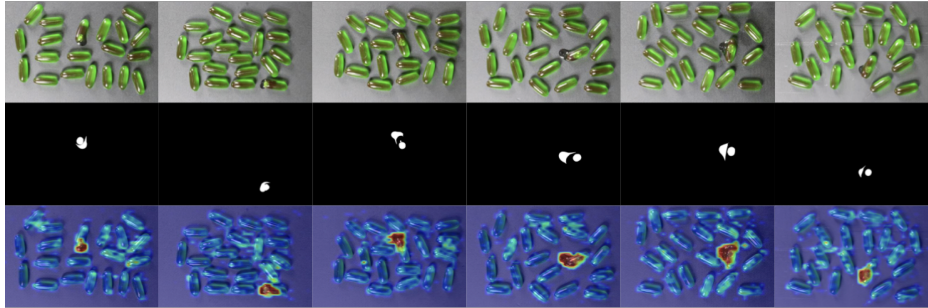


Figure 11. The visualization highlights the **capsule** object from the VisA dataset, while the model is trained on the MVTec-AD dataset. The first row represents the input, the second row shows the ground truth segmentation mask. The last row presents the segmentation results from DAPO. Despite the distribution shift, our model accurately localizes both **leak** and **bubble** defects. Notably, the image contains multiple defects, demonstrating the model’s capability to segment multiple anomalies within a single sample.

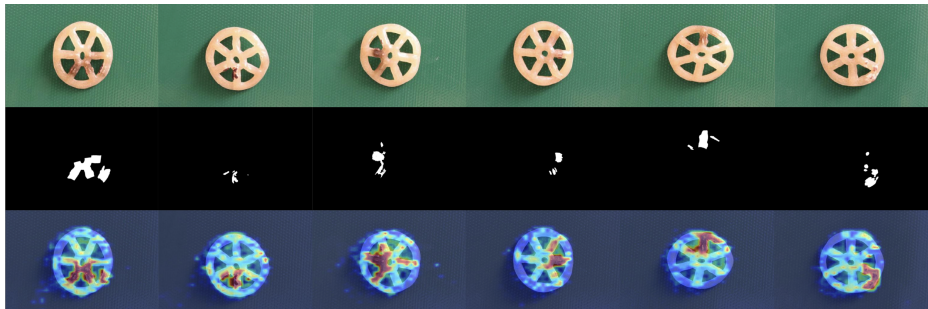


Figure 12. The visualization highlights the **Fryum** object from the VisA dataset, with the model trained on MVTec-AD. As shown, DAPO successfully localizes the **burnt** defect, however the segmentation slightly overextends beyond the actual defect region, indicating minor over-segmentation.

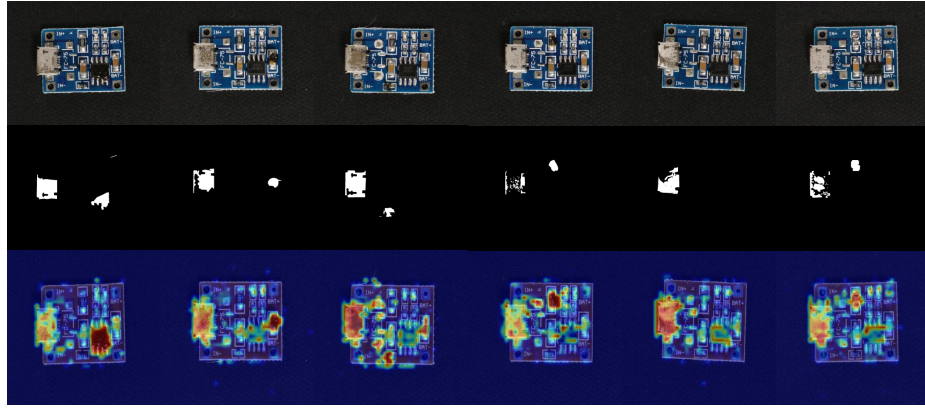


Figure 13. The visualization highlights the **PCB4** object from the VisA dataset, with the model trained on MVTec-AD. As shown, DAPO successfully localizes both the **burnt** and **dirt** defects within the same image. However, it fails to detect a small **scratch** defect in the top-right corner of the first image, likely due to the patch-level features being unable to effectively capture such fine-grained anomalies.

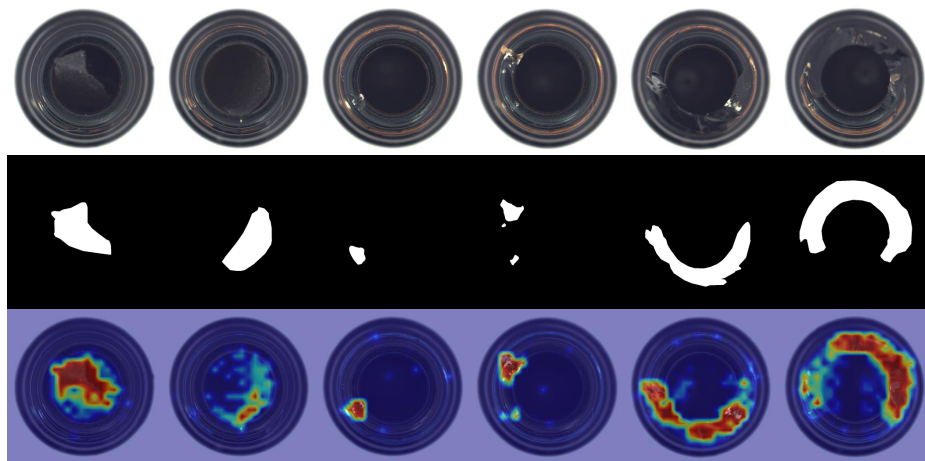


Figure 14. The visualization highlights the **Bottle** object from the MVTec-AD dataset, with the model trained on VisA. Columns 1–2 show localization of the **contamination** defect, 3–4 capture the **small break**, while 5–6 successfully segment **large break**.

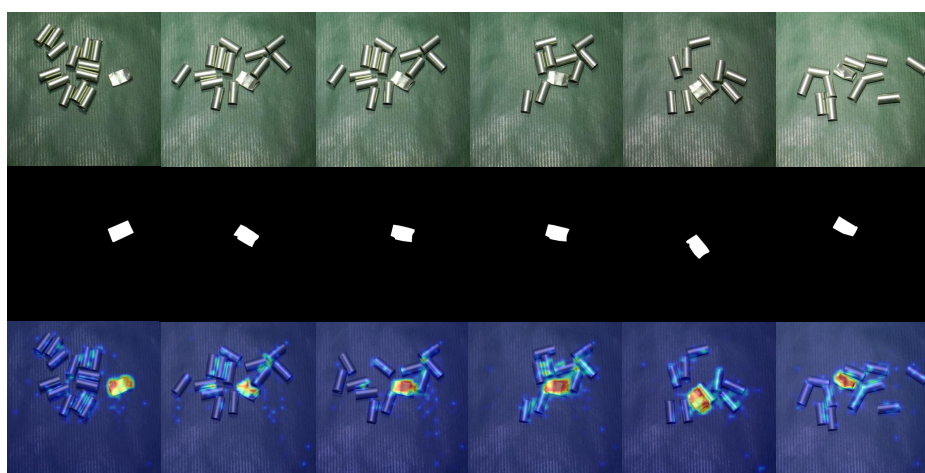


Figure 15. The visualization highlights the **Tubes** object from the MPDD dataset. The model, trained on MVTec-AD, accurately localizes the **flattening** defect with minimal noise, demonstrating its precision in segmenting flattening defects, as evident from Table 13.

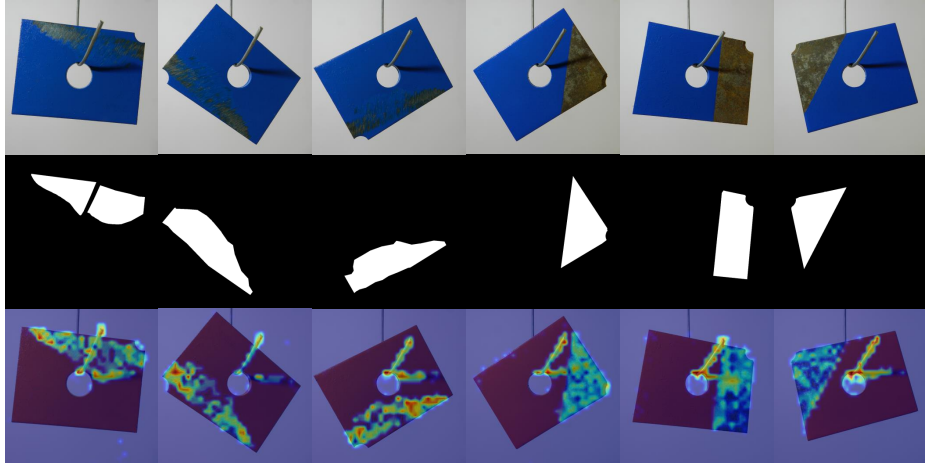


Figure 16. The visualization highlights the **Metal Plate** object from the MPDD dataset. Columns 1–3 show accurate localization of the **scratch** defect, while columns 4–6 demonstrate precise segmentation of the **rust** defect.

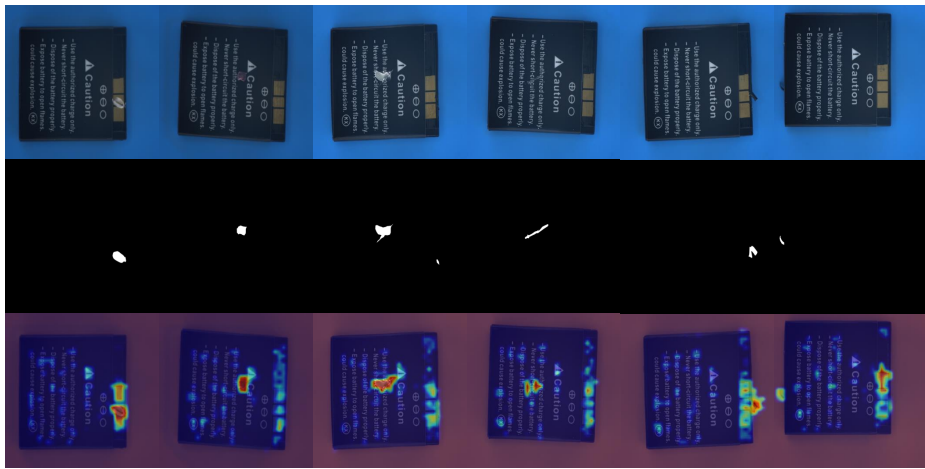


Figure 17. The visualization shows the **Phone Battery** object from the Real-IAD dataset. Our model accurately localizes both **scratch** and **damage** defects.

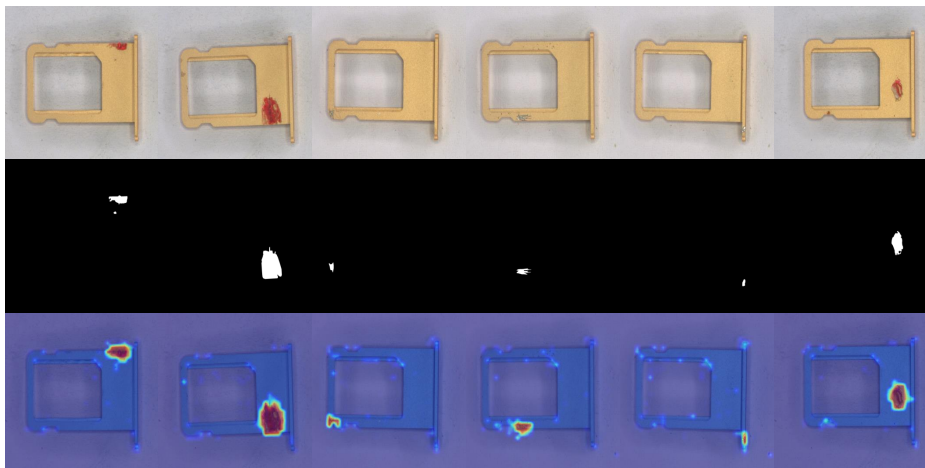


Figure 18. The visualization highlights the **SIM Card Set** object from the Real-IAD dataset. DAPO successfully segments the **scratch** defect with clear localization.

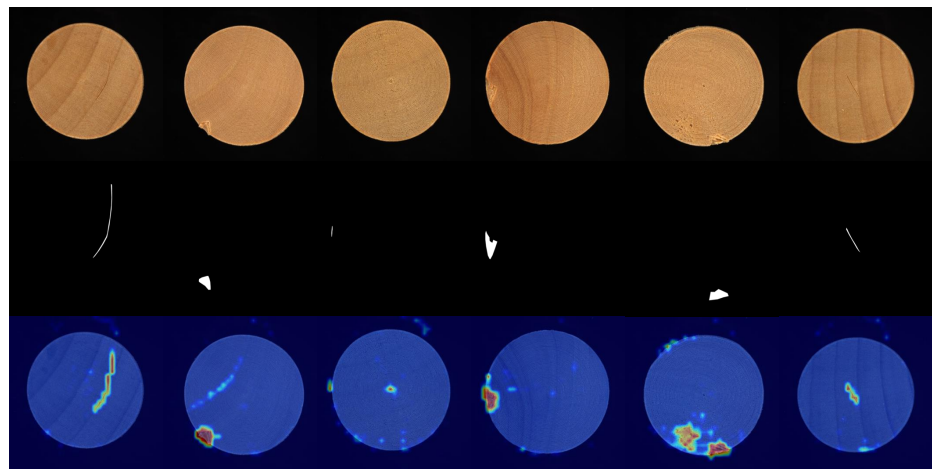


Figure 19. The visualization depicts the **Firewood** object from the Real-IAD dataset. Our model effectively localizes both **scratch** and **damage** defects, despite the irregular surface texture.